

Gas-driven tensile fracturing in shallow marine sediments

Hugh Daigle¹, Ann Elizabeth Cook², Yi Fang³, Abhishek Bihani¹, Wen Song¹, and Peter B. Flemings⁴

¹University of Texas at Austin

²Ohio State University

³The University of Texas at Austin

⁴Department of Geological Sciences & Institute for Geophysics

November 24, 2022

Abstract

The flow of gas through shallow marine sediments is an important component of the global carbon cycle and affects methane release to the ocean and atmosphere as well as submarine slope stability. Seafloor methane venting is often linked to dissociating hydrates or gas migration from a deep source, and subsurface evidence of gas-driven tensile fracturing is abundant. However, the physical links among hydrate dissociation, gas flow, and fracturing has not been rigorously investigated. We used mercury intrusion data to model the capillary drainage curves of shallow marine muds as a function of clay content and porosity. We combined these with estimates of in situ tensile strength to determine the critical gas saturation at which the pressure of the gas phase would exceed the pressure required to generate tensile fractures. Our work demonstrates that tensile fracturing is more likely as clay content increases due to decreased pore sizes and increased capillary pressure, but tends to be restricted to the shallowest portion of the sediment column (<130 m below seafloor) except when the clay-sized fraction exceeds 50%. Dissociating hydrate may supply sufficient quantities of gas to cause fracturing, but this is only likely near the updip limit of the hydrate stability zone, where release of methane bubbles from discrete vents is to be expected due to the combination of weak sediments and significant gas expansion. Gas-driven tensile fracturing is probably a common occurrence near the seafloor, does not require much gas, and is not necessarily an indication of hydrate dissociation.

1 **Gas-driven tensile fracturing in shallow marine sediments**

2 Hugh Daigle^{1,2*}, Ann Cook³, Yi Fang⁴, Abhishek Bihani^{1,2}, Wen Song^{1,2}, and Peter B.

3 Flemings^{4,5}

4 ¹Center for Subsurface Energy and the Environment, The University of Texas at Austin, Austin,
5 TX, 78712

6 ²Hildebrand Department of Petroleum and Geosystems Engineering, The University of Texas at
7 Austin, Austin, TX, 78712

8 ³School of Earth Sciences, The Ohio State University, Columbus, OH, 43210

9 ⁴Institute for Geophysics, Jackson School of Geosciences, The University of Texas at Austin,
10 Austin, TX, 78712

11 ⁵Department of Geological Sciences, Jackson School of Geosciences, The University of Texas at
12 Austin, Austin, TX, 78712

13 *Corresponding author. Email: daigle@austin.utexas.edu

14

15

16

17

18

19

20

21

22

23

24 Key points

- 25 • Gas-driven tensile fracturing can occur easily in near-seafloor sediments
- 26 • If the clay-sized fraction exceeds 60-70%, gas saturations <10% can generate tensile
- 27 fractures in sediments as deep as 2 km below seafloor
- 28 • Hydrate dissociation can cause fracturing and venting near the updip limit of hydrate
- 29 stability, but is not the only source of vented gas

30

31

32

33

34

35

36

37

38

39

40

41

42

43

44

45

46

47 Abstract

48 The flow of gas through shallow marine sediments is an important component of the
49 global carbon cycle and affects methane release to the ocean and atmosphere as well as
50 submarine slope stability. Seafloor methane venting is often linked to dissociating hydrates or
51 gas migration from a deep source, and subsurface evidence of gas-driven tensile fracturing is
52 abundant. However, the physical links among hydrate dissociation, gas flow, and fracturing has
53 not been rigorously investigated. We used mercury intrusion data to model the capillary drainage
54 curves of shallow marine muds as a function of clay content and porosity. We combined these
55 with estimates of in situ tensile strength to determine the critical gas saturation at which the
56 pressure of the gas phase would exceed the pressure required to generate tensile fractures. Our
57 work demonstrates that tensile fracturing is more likely as clay content increases due to
58 decreased pore sizes and increased capillary pressure, but tends to be restricted to the shallowest
59 portion of the sediment column (<130 m below seafloor) except when the clay-sized fraction
60 exceeds 50%. Dissociating hydrate may supply sufficient quantities of gas to cause fracturing,
61 but this is only likely near the updip limit of the hydrate stability zone, where release of methane
62 bubbles from discrete vents is to be expected due to the combination of weak sediments and
63 significant gas expansion. Gas-driven tensile fracturing is probably a common occurrence near
64 the seafloor, does not require much gas, and is not necessarily an indication of hydrate
65 dissociation.

66 *Keywords:* hydrates, fracturing, gas, marine sediments

67

68

69

70 Plain language summary

71 Gas bubble emissions from discrete locations on the seafloor are observed at many
72 locations worldwide. Bubble emissions are often be linked to hazards such as submarine
73 landslides and may contribute to ocean acidification and release of methane and carbon dioxide
74 to the atmosphere. Observations indicate that the gas tends to move through fractures or cracks,
75 but the role of gas in potentially forming those fractures and the overall process of gas
76 accumulation and flow in shallow marine sediments are not well understood. Using a new model
77 based on laboratory data to predict how much gas is needed to generate fractures in shallow
78 marine sediments, we show that gas can easily generate fractures near the seafloor, particularly
79 when the sediments contain a significant amount of clay. Our results demonstrate that gas-driven
80 fracturing is probably a common occurrence near the seafloor, does not require very much gas,
81 and may not necessarily be an indication of gas hydrate melting caused by ocean temperature
82 increase.

83

84 1. Introduction

85 Methane hydrates are ice-like, non-stoichiometric compounds of water and methane that
86 are stable at high pressure and low temperatures, and occur in the shallow subsurface of
87 continental margins and in sediments below permafrost [*Ruppel, 2011*]. There are three research
88 foci associated with methane hydrates: (1) as an energy resource, (2) as a large reservoir of
89 carbon with associated roles in climate change and carbon cycling, and (3) as a potential marine
90 geohazard [*Maslin et al., 2010; Boswell and Collett, 2011; Collett et al., 2015; Ruppel and*
91 *Kessler, 2017*]. The geomechanical aspects of methane hydrate formation and associated gas
92 migration in marine sediments has been an active area of research for many years [e.g., *Flemings*

93 *et al.*, 2003; *Nimblett and Ruppel*, 2003; *Hornbach et al.*, 2004; *Xu and Germanovich*, 2006; *Jain*
94 *and Juanes*, 2009; *Daigle and Dugan*, 2010b; *Fauria and Rempel*, 2011; *Stranne et al.*, 2017].
95 Particular interest has been given to hydrate that occurs as a filling in fractures and veins
96 [*Nimblett and Ruppel*, 2003; *Cook and Goldberg*, 2008; *Cook et al.*, 2008; *Daigle and Dugan*,
97 2010b; *Daigle and Dugan*, 2011; *Cook et al.*, 2014; *Jin et al.*, 2015]. These features tend to occur
98 predominantly in clay-rich sediments, suggesting that they are related to low permeability and
99 associated elevated fluid pressures [*Ginsburg and Soloviev*, 1997; *Sassen et al.*, 2001;
100 *Weinberger and Brown*, 2006; *Daigle and Dugan*, 2010b; *Daigle and Dugan*, 2011], or that they
101 form as a result of capillary forces inhibiting nucleation of disseminated hydrate within the pore
102 space [*Clennell et al.*, 1999; *Rempel*, 2011; *Cook et al.*, 2014; *You et al.*, 2019]. The prospect that
103 marine sediments may fail in tension or shear due to pore pressures associated with fluid flow
104 and methane hydrate dissociation has significant implications for hydrates as a geohazard and
105 release of methane to the water column.

106 Gas-driven tensile fracturing in association with methane hydrates has been investigated
107 or suggested by many authors [*Wood et al.*, 2002; *Flemings et al.*, 2003; *Natzeband et al.*, 2005;
108 *Zühlsdorff and Spiess*, 2004; *Liu and Flemings*, 2007; *Hustoft et al.*, 2009; *Jain and Juanes*,
109 2009; *Daigle and Dugan*, 2010a; *Choi et al.*, 2011; *Daigle et al.*, 2011; *Holtzman and Juanes*,
110 2011; *Rees et al.*, 2011; *Sun et al.*, 2012; *Sultan et al.*, 2014; *Stranne et al.*, 2017]. Fractures are
111 high-permeability conduits that can lead to venting of methane at the seafloor [e.g., *Hustoft et al.*,
112 2009], and the ability of gas generated from hydrate dissociation to fracture overlying sediments
113 has important implications for predicting feedbacks between ocean warming and methane release
114 [e.g., *Archer et al.*, 2009]. Issues relating to gas-driven tensile fracturing extend to marine
115 sediments outside the hydrate stability zone as well, with the movement of gas posing hazards to

116 offshore infrastructure and contributing to sediment-ocean methane exchange [Best et al., 2006].
117 The importance of gas-driven fracturing to shallow gas movement is overall poorly understood
118 due to a lack of predictive models [James et al., 2016].

119 We used high-pressure mercury intrusion (HPMI) measurements performed on marine
120 sediments from around the world to constrain relationships between capillary pressure and gas
121 saturation, and combined this with estimates of tensile strength to predict the conditions under
122 which gas-driven tensile failure may occur. We show that any amount of gas will cause
123 fracturing in sediments as deep as 500 m below sea floor (mbsf) if the fraction of clay-sized
124 grains is larger than 70%, while fracturing will only occur in sediment shallower than 100 mbsf
125 when the clay-sized fraction exceeds 20%. The predictive model we present for variation in
126 capillary pressure curves with porosity and clay-sized fraction allows for detailed predictions of
127 sealing capacity and mode of gas migration in heterogeneous lithologies. We finally demonstrate
128 that hydrate dissociation near the landward limit of the hydrate stability zone can easily lead to
129 gas-driven tensile fracturing and bubble emission.

130

131 2. Tensile fracturing and capillary drainage

132 In a saturated porous medium, tensile failure will occur when the fluid pressure exceeds
133 the sum of the minimum principal stress (σ_3) and the tensile strength of the medium (T) [Jain and
134 Juanes, 2009; Boudreau, 2012] (all nomenclature is defined in Table 1). In a water-wet porous
135 medium, a gas phase will always exist at a greater pressure than the water phase, with the
136 pressure difference equal to the capillary pressure. In this situation, the gas phase will tend to be
137 the phase initiating fracturing. The fracturing criterion can thus be written as

138

139 $P_g > \sigma_3 + T,$ (Eq. 1)

140

141 where P_g is the gas phase pressure. Here, T is assumed to be positive as it represents a strength
142 rather than a stress. Eq. 1 may be recast in terms of the capillary pressure P_c by subtracting the
143 water phase pressure P_w from both sides:

144

145 $P_g - P_w = P_c > \sigma_3 - P_w + T.$ (Eq. 2)

146

147 Note that the presence of two immiscible fluid phases requires the use of total, rather than
148 effective, stress in Eqs. 1 and 2, since stress transfer across fluid-fluid interfaces changes the
149 thermodynamic considerations of the relationships between fluid phase pressures and the
150 deformation of the porous medium [*Bishop, 1959; Coussy, 2004, 2007; Nuth and Laloui, 2008;*
151 *Boudreau, 2012*]. Indeed, if a thin film of water separates gas from the grain surface as expected
152 in a water-wet medium [*Hirasaki, 1991*], the gas-phase pressure can only act on the rock through
153 the water film, causing a local increase in the water-phase pressure. The use of the total stress
154 removes the need to consider this effect. Eq. 2 thus establishes a fracture criterion based on
155 capillary pressure.

156 The capillary pressure of the gas phase is related to the volume fraction of the pore space
157 occupied by gas, which is the gas saturation S_g . As a nonwetting phase, gas must overcome an
158 entry pressure for the curved gas-water interface to enter a pore and displace water. For a
159 cylindrical pore of radius r , the entry pressure P_e for a completely nonwetting fluid is given by
160 Washburn's equation [*Washburn, 1921*]:

161

162 $P_e = \frac{2\gamma}{r},$ (Eq. 3)

163

164 where γ is the gas-water interfacial tension. Because sediments contain a range of pore sizes,
165 different values of gas pressure will correspond to gas entering pores of different sizes. The
166 capillary drainage curve describes the relationship between gas pressure and gas saturation with
167 the assumption that gas will fill the largest pores at the lowest pressures and move into
168 progressively smaller pores with increasing pressure [Bear, 1972]. During primary drainage,
169 wherein the sediment begins fully saturated with water, gas must first overcome the entry
170 pressure of the largest pores. After that, with each pressure increment it will displace water from
171 any pore that has an entry pressure smaller than or equal to the new capillary pressure and has a
172 connected pathway to existing gas-filled pores [Larson and Morrow, 1981]. The value of P_c that
173 satisfies the tensile fracturing criterion in Eq. 2 may therefore be related to a critical gas
174 saturation through the capillary drainage curve.

175 The potential for tensile fracturing due to excess gas pressure can be reduced if the gas
176 pressure can dissipate by porous flow. Flow of a nonwetting phase in a porous medium can only
177 occur if the gas saturation achieves a certain mobility threshold saturation. The mobility
178 threshold depends on many different properties of the sediment, including pore structure and
179 scale of heterogeneities. While numerical and laboratory pore network models have
180 demonstrated that nonwetting phase flow occurs only after the saturation achieves the
181 percolation threshold [Chatzis and Dullien, 1977; Larson and Morrow, 1981; Lenormand et al.,
182 1983; Diaz et al., 1987; Ewing and Gupta, 1993; Sahimi, 2011], experiments on real muds and
183 mudrocks have shown gas breakthrough at saturations far below the percolation threshold.
184 Schowalter [1979] suggested a mobility threshold of 10%, while the experiments of Hildenbrand

185 *et al.* [2002; 2004] suggest a much lower value around 2%. If the mobility threshold is reached
186 before tensile failure occurs, then pressure can be dissipated by porous flow. The exception to
187 this is the case where the rate of pressure buildup exceeds the rate of dissipation to the point
188 where tensile fracture occurs. We note that our treatment of gas-driven tensile failure considers
189 the coexistence of a wetting and nonwetting phase within a representative elementary volume of
190 a porous medium. We are not considering dynamics of gas ganglia, thin fluid films, or other
191 processes operating at the grain or pore scale. Since the capillary drainage curve is a macroscopic
192 description of the relationship between nonwetting phase pressure and saturation [Bear, 1972],
193 our approach to the fracturing criterion should be valid. More sophisticated models are needed to
194 examine behavior at the grain scale [e.g., Jain and Juanes, 2009; Bihani and Daigle, 2019].

195 Finally, we note that we do not consider fracture propagation or any dynamic mechanical
196 response after the fracturing criterion is met. Johnson *et al.* [2002] and Barry *et al.* [2010],
197 among others, have shown that tensile failure and gas bubble rise in shallow marine sediments is
198 described well by linear elastic fracture mechanics (LEFM). There are two pertinent items
199 related to fracturing behavior. First, Algar *et al.* [2011] and Boudreau [2012] have shown that,
200 after gas initially opens a fracture that then closes, subsequent gas escape will occur
201 preferentially by reactivating the existing fracture surface. The fracture criterion we adopt in this
202 work corresponds to initial fracturing, but it is important to remember that subsequent fracturing
203 will be much easier and occur at lower gas pressures and saturations. Second, the opening of a
204 tensile fracture compresses the surrounding, unfailed sediment, which inhibits additional tensile
205 fracturing in the immediate vicinity of the original fracture due to the local increase in horizontal
206 stress. This phenomenon is known as the stress shadow effect [Warpinski and Teufel, 1987;
207 Warpinski and Branagan, 1989]. Tensile fractures will therefore have a characteristic spacing

208 that is related to the material properties of the host sediments. This in turn may limit the gas flow
209 rate as fracture spacing controls fracture system permeability along with fracture aperture
210 [Daigle and Dugan, 2010b].

211

212 3. Methods

213 Determining the potential for gas-driven tensile fracturing requires (1) an estimate of in
214 situ stresses, (2) an estimate of tensile strength, and (3) a capillary drainage curve. An illustration
215 of this process with relevant parameters is shown in Fig. 1.

216

217 *3.1 In situ stress estimation*

218 We considered a generic marine sedimentary setting where the maximum principal stress
219 was vertical (σ_v), and the sediments were vertically transversely isotropic such that the two
220 horizontal stresses were equal to the minimum principal stress σ_h . We emphasize here that these
221 are far-field stresses and not subject to any local perturbations that may arise from the presence
222 of gas. Defining the vertical and horizontal effective stresses as $\sigma_v' = \sigma_v - P_w$ and $\sigma_h' = \sigma_h - P_w$
223 where P_w is the porewater pressure, from linear elasticity

224

$$225 \sigma_h' = \frac{\nu}{1-\nu} \sigma_v', \quad (\text{Eq. 4})$$

226

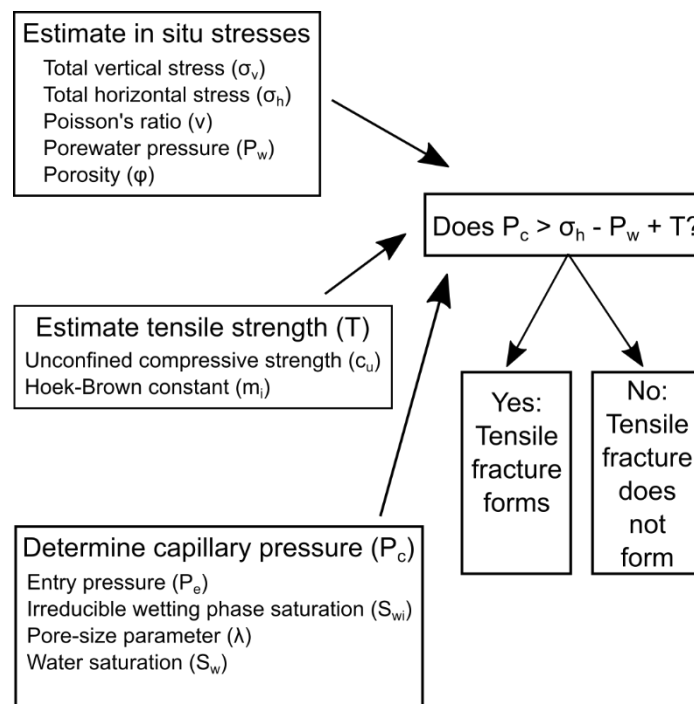
227 or

228

$$229 \sigma_h = \frac{\nu}{1-\nu} (\sigma_v - P_w) + P_w, \quad (\text{Eq. 5})$$

230

231 where ν is Poisson's ratio. We acknowledge that there is longstanding disagreement in the
 232 literature as to how well Eqs. 4 and 5 represent the true in situ stresses in shallow marine
 233 sediments (see the discussion in *Zoback* [2007]). For example, *Eaton* [1969] used drilling data
 234 from the Gulf of Mexico to back-calculate Poisson's ratio from Eq. 4 and found that $\nu < 0.3$ was
 235 necessary to fit the data in the shallowest sediments. These values of ν are much lower than
 236 typical values for shallow sediments (>0.4 [*Hamilton, 1979; Reynolds, 1997*]). On the other
 237 hand, leak-off test data from shallow sediments in the Gulf of Mexico [*Wojtanowicz et al., 2000*]
 238 and the South China Sea [*Yan et al., 2015*] indicate that the minimum horizontal stress is very
 239 close to the vertical stress ($\sigma_h'/\sigma_v' > 0.8$) which is more consistent with expected values of ν (i.e.,
 240 $\sigma_h'/\sigma_v' = 0.8$ implies $\nu = 0.44$ from Eq. 4). Our use of Eqs. 4 and 5 is therefore consistent with
 241 evidence in the literature. If σ_h is overestimated, the result in our model will simply be that gas-
 242 driven tensile fracturing will be more likely.



243
 244 **Figure 1.** Illustration of process for determining the potential for tensile failure with relevant
 245 parameters.

246 We used the relationship reported by *Kominz et al.* [2011] for clay to determine porosity
247 φ as a function of depth below seafloor z (m):

248

249

$$250 \quad \varphi = 0.775e^{-\frac{z}{1251}}. \quad (\text{Eq. 6})$$

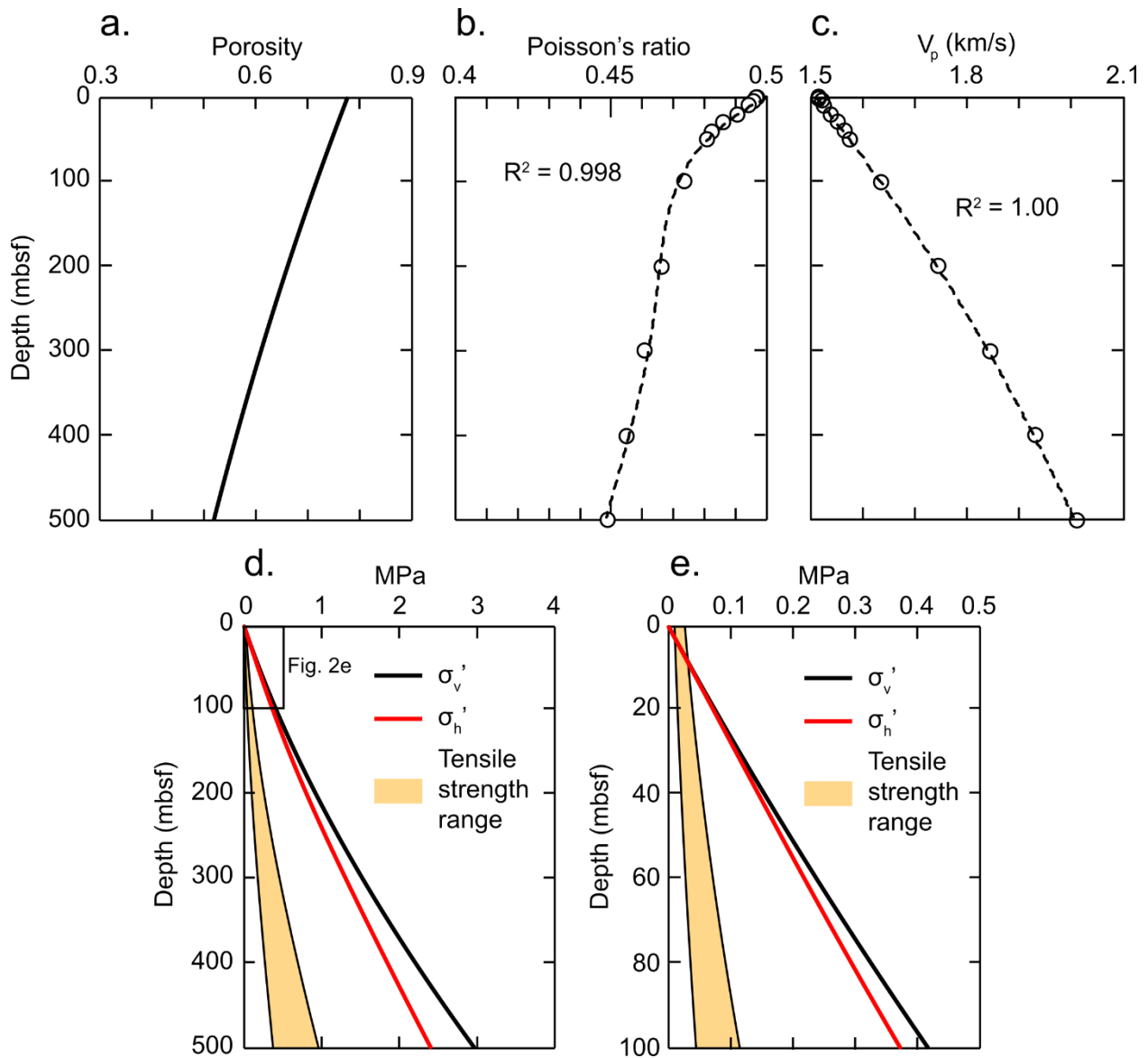
251

252 Note that this differs from the form of the equation given by *Kominz et al.* [2011] as it has been
253 modified to yield porosity in decimal rather than percent. Eq. 6 is valid for sediments shallower
254 than 500 m below seafloor (mbsf) (Fig. 2a). We then determined the bulk density as a function of
255 depth from the porosity with pore fluid density of 1024 kg/m^3 and sediment grain density of
256 2700 kg/m^3 . The vertical effective stress was then calculated by integrating the bulk density with
257 respect to depth with an assumption of hydrostatic pore pressure. To find σ_h , we determined v as
258 a function of depth by fitting a 6th-order polynomial to *Hamilton's* [1979] compilation of v in
259 shallow marine sediments, and the total vertical stress was obtained from porosity or bulk
260 density data (Fig. 2b).

261

262 *3.2 Tensile strength estimation*

263 In the framework of *Griffith* [1921], marine sediments may be considered as media filled
264 with a number of existing flaws that increase in size and coalesce during fracturing. One method
265 of obtaining the tensile strength in this framework is to determine the mode I fracture toughness
266 and make an assumption of initial flaw size, thus determining the tensile strength using LEFM.
267 Many studies have shown that this method can accurately describe the fracture initiation and
268 propagation processes in marine sediments [*Johnson et al.*, 2002; *Boudreau et al.*, 2005; *Algar*



269

270 **Figure 2.** (a) Porosity-depth curve from *Kominz et al.* [2011]. (b) Polynomial fit for Poisson's
 271 ratio versus depth. (c) Polynomial fit for compressional wave velocity (V_p) versus depth. Data
 272 shown in (b) and (c) from *Hamilton* [1979]. (d) Vertical and horizontal effective stresses along
 273 with range of tensile strength for our generic passive margin sediments. (e) Close-up of (d)
 274 showing behavior at shallow depths.

275

276

277

278

279

280 *and Boudreau, 2010; Barry et al., 2010; Johnson et al., 2012*]. However, as *Boudreau [2012]*
281 points out, the initial flaw size in marine sediments is usually unknown, which presents serious
282 challenges in using LEFM as a predictive tool for tensile strength. Therefore, we adopted a
283 simpler method of determining tensile strength based on the Hoek-Brown failure criterion [*Hoek*
284 *and Brown, 1997*].

285 The Hoek-Brown failure criterion is an empirically derived, nonlinear Mohr-Coulomb
286 failure envelope. For intact rocks, the tensile strength T is related to the unconfined compressive
287 strength c_u by

$$288 \quad T = -\frac{c_u}{2} \left(m_i - \sqrt{m_i^2 + 4} \right), \quad (\text{Eq. 7})$$

289
290 where m_i is the Hoek-Brown constant. *Hoek [2006]* gives a recommended value of $m_i = 4 \pm 2$ for
291 claystones, and this value is consistent with results of triaxial shear experiments performed on
292 marine muds and mudstones by *Silva et al. [2000]*, *Moses et al. [2003]*, *Dugan and Germaine*
293 *[2009]*, and *Schumann et al. [2014]*. Therefore we used this value for m_i . To determine c_u , we
294 used the correlation of *Ingram and Urai [1999]* for muds and mudrocks:

$$295 \quad \log_{10} c_u = -6.36 + 2.45 \log_{10}(0.86V_p - 1172), \quad (\text{Eq. 8})$$

296
297 where c_u is given in MPa and V_p is compressional wave velocity in m/s. The vertical and
298 horizontal effective stresses, as well as the range of tensile strength predicted from Eq. 7, are
299 shown in Figs. 2d and 2e. Tensile strength ranges from 18.1 ± 7.92 kPa at the sea floor to
300 679 ± 297 kPa at 500 mbsf (with uncertainties corresponding to the possible range of m_i). The
301
302

303 average value at 500 mbsf is 28% of the horizontal effective stress, and this ratio is relatively
304 constant at 21-28% from 30 to 500 mbsf, above which the tensile strength corresponds to a
305 greater fraction of the horizontal effective stress.

306

307 3.3 Capillary drainage curves

308 We used the Brooks-Corey parameterization of the capillary drainage curve:

309

$$310 P_c(S_w) = P_e \left(\frac{S_w - S_{wi}}{1 - S_{wi}} \right)^{-\frac{1}{\lambda}}, \quad (\text{Eq. 9})$$

311

312 where S_w is the wetting phase saturation (assumed to be water), S_{wi} is the irreducible wetting
313 phase saturation, P_e is the capillary entry pressure, and λ is the pore-size parameter [Brooks and
314 Corey, 1964]. To constrain the Brooks-Corey parameters (P_e , S_{wi} , and λ), we used previously
315 published mercury intrusion capillary pressure (MICP) performed on natural and resedimented
316 samples of marine muds from various locations around the world [Daigle and Dugan, 2014;
317 Daigle et al., 2019]. The Brooks-Corey parameters are expected to vary with grain size and
318 porosity. We found the following correlations for P_e and λ :

319

$$320 \ln P_e = (6.59 \pm 0.584)(1 - \varphi + S_{wi})f_c - (2.76 \pm 0.224), \quad (\text{Eq. 10})$$

321

322 where P_e is in MPa, φ is total porosity (determined independently for all samples by the
323 moisture-and-density method), and f_c is the mass fraction of the solid matrix composed of clay-
324 sized grains (smaller than 2 μm in diameter). Eq. 10 calculates P_e for methane invading a water-
325 saturated pore, while the pressures measured in the MICP tests corresponded to mercury entering

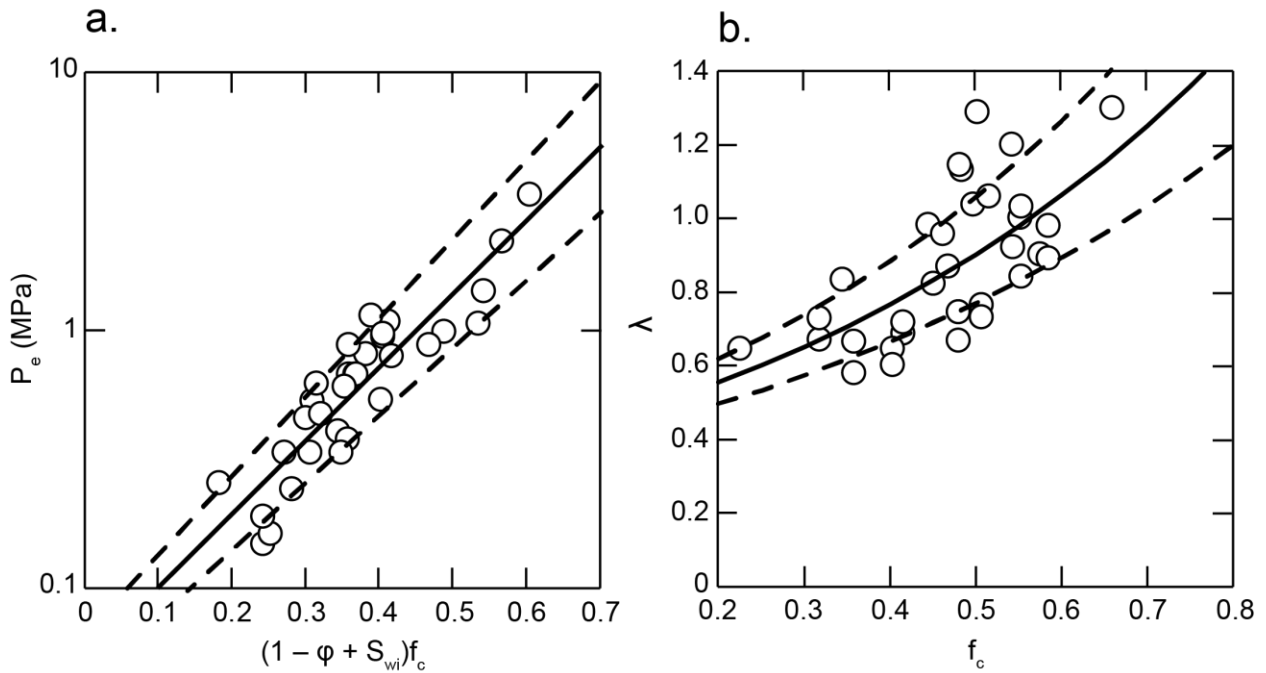
326 an evacuated pore. The mercury pressures were converted to equivalent methane-water pressures
 327 by multiplying by $-(\gamma_{\text{CH}_4,\text{W}}\cos\theta_{\text{CH}_4,\text{W}})/(\gamma_{\text{Hg},\text{V}}\cos\theta_{\text{Hg},\text{V}})$ where $\gamma_{\text{CH}_4,\text{W}}$ is the methane-water
 328 interfacial tension (0.072 N/m), $\theta_{\text{CH}_4,\text{W}}$ is the contact angle of the methane-water interface on
 329 solid grains (0°) [Henry *et al.*, 1999], $\gamma_{\text{Hg},\text{V}}$ is the mercury-vacuum interfacial tension (0.480
 330 N/m), and $\theta_{\text{Hg},\text{V}}$ is the contact angle of the mercury-vacuum interface on solid grains (140°)
 331 [Purcell, 1949]. The minus sign in this expression is necessary since $\cos\theta_{\text{Hg},\text{V}} < 0$. The
 332 correlation for the pore-size parameter was found to be

$$334 \quad \ln \lambda = (1.64 \pm 0.162)f_c - (0.921 \pm 0.0774). \quad (\text{Eq. 11})$$

335
 336 These correlations had R^2 of 0.81 and 0.46, respectively (Fig. 3). The reported errors in the
 337 regression coefficients are ± 1 standard deviation.

338 The S_{wi} determined from an MICP test is not the true irreducible wetting phase saturation
 339 (i.e., the wetting phase volume fraction trapped irretrievably by capillary forces) because during
 340 the MICP test mercury (assumed to be the nonwetting phase) displaces air or vacuum (assumed
 341 to be the wetting phase). Therefore, some independent estimate of S_{wi} is necessary to be able to
 342 predict the behavior of a gas-water system. Daigle *et al.* [2015] showed that the volume of clay-
 343 bound water in marine muds can be determined from porosity and fraction of clay-sized ($< 2 \mu\text{m}$)
 344 grains. Since S_{wi} represents the amount of water remaining in the pore system at infinite capillary
 345 pressure, the amount of clay-bound water can be used as a reasonable proxy. Therefore we
 346 determined S_{wi} following Daigle *et al.* [2015] as

$$347 \quad S_{wi} = (0.326 \pm 0.0220)f_c^{0.219 \pm 0.103} + (0.0262 \pm 0.00915)/\phi, \quad (\text{Eq. 12})$$



350

351 **Figure 3.** (a) Correlation for predicting entry pressure. (b) Correlation for predicting λ . Solid
 352 lines in both plots are best fit, while the dashed lines are ± 1 standard deviation.

353

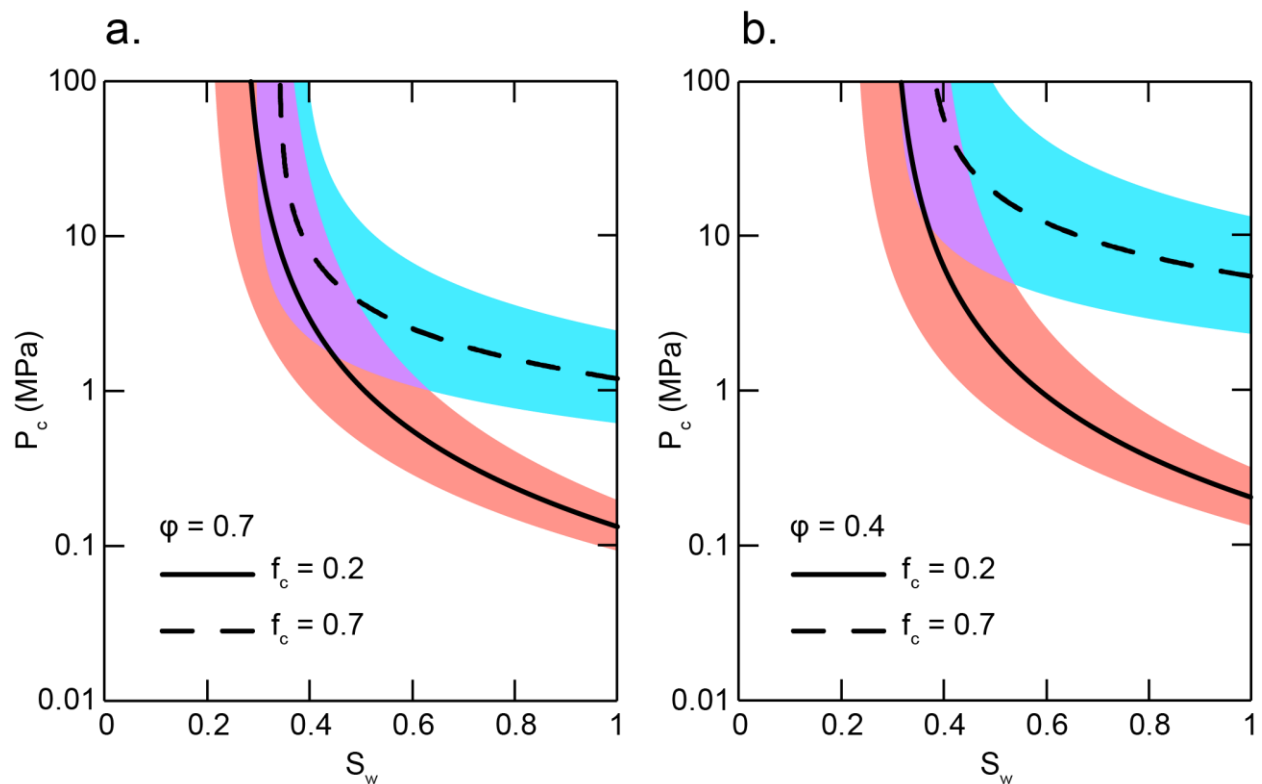
354 where the reported errors are ± 1 standard deviation. The Brooks-Corey capillary drainage curves
 355 with parameters determined from Eqs. 10-12 are shown in Figure 4 for $\phi = 0.7$ and 0.4 and $f_c =$
 356 0.7 and 0.2 . Our approach differs from that of *Leverett* [1941] in that knowledge of permeability
 357 is not necessary. Indeed, formulating the capillary pressure curve in terms of porosity and clay-
 358 size fraction allows more direct facies-based prediction using empirical models that are specific
 359 to shallow marine sediments.

360

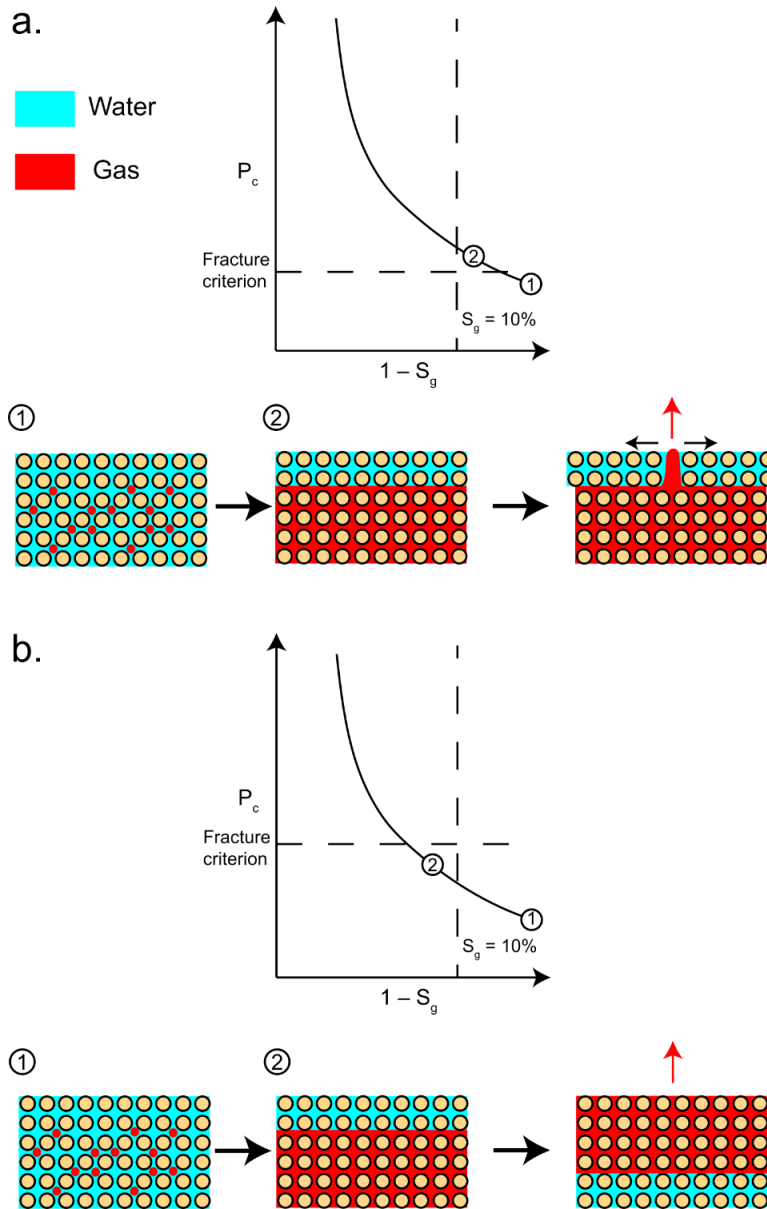
361 *3.4 Fracture versus flow*

362 Gas will migrate by porous flow instead of initiating tensile fractures if it achieves the
 363 mobility threshold at a capillary pressure below the fracturing criterion given by Eq. 2 and the
 364 intrinsic sediment permeability and gas-phase relative permeability are large enough to allow

365 flow without additional pressure buildup. Based on the work of *Schowalter* [1979], we assumed
 366 a mobility threshold gas saturation of 10%, where the gas saturation $S_g = 1 - S_w$. If the fracturing
 367 criterion is achieved at gas saturations lower than this value, then tensile fracturing will occur
 368 before porous flow (Fig. 5a). If the capillary pressure at 10% gas saturation is smaller than the
 369 fracture criterion, this does not necessarily preclude tensile fracturing. Rather, it indicates that a
 370 rapid, transient increase in gas saturation would be required to generate fractures, as this could
 371 allow the gas pressure to reach the fracture criterion before being dissipated by porous flow (Fig.
 372 5). Note that using a 10% mobility threshold will give more conservative estimates of fracturing
 373 behavior than using the percolation threshold, which is considerably larger than 10% in shallow
 374



375
 376 **Figure 4.** Predicted capillary drainage curves for porosities of 0.7 (a) and 0.4 (b) at clay fractions
 377 of 0.2 and 0.7. The shaded regions represent the overall uncertainty based on the uncertainties of
 378 the input parameters.
 379



382 **Figure 5.** (a) Capillary pressure at the fracture criterion corresponding to a gas saturation smaller
 383 than the mobility threshold. At point 1, gas (red) starts accumulating in the sediment. This could
 384 be due to local microbial methanogenesis, hydrate dissociation, or buoyant migration of discrete
 385 bubbles from a deeper source. The gas continues accumulating to a gas saturation and capillary
 386 pressure represented by point 2. At this point, the fracture criterion is exceeded and the gas opens
 387 a tensile fracture, allowing buoyant migration. (b) Capillary pressure at the fracture criterion
 388 corresponding to a gas saturation larger than the mobility threshold. Gas starts accumulating
 389 (point 1) to a saturation and capillary pressure corresponding to point 2. Since this saturation is
 390 larger than the mobility threshold and the capillary pressure is smaller than the fracture criterion,
 391 the gas can move by porous flow.

392 marine muds [Daigle et al., 2019]. Future research should investigate gas mobility thresholds
393 specific to marine muds, and how this threshold varies during burial.

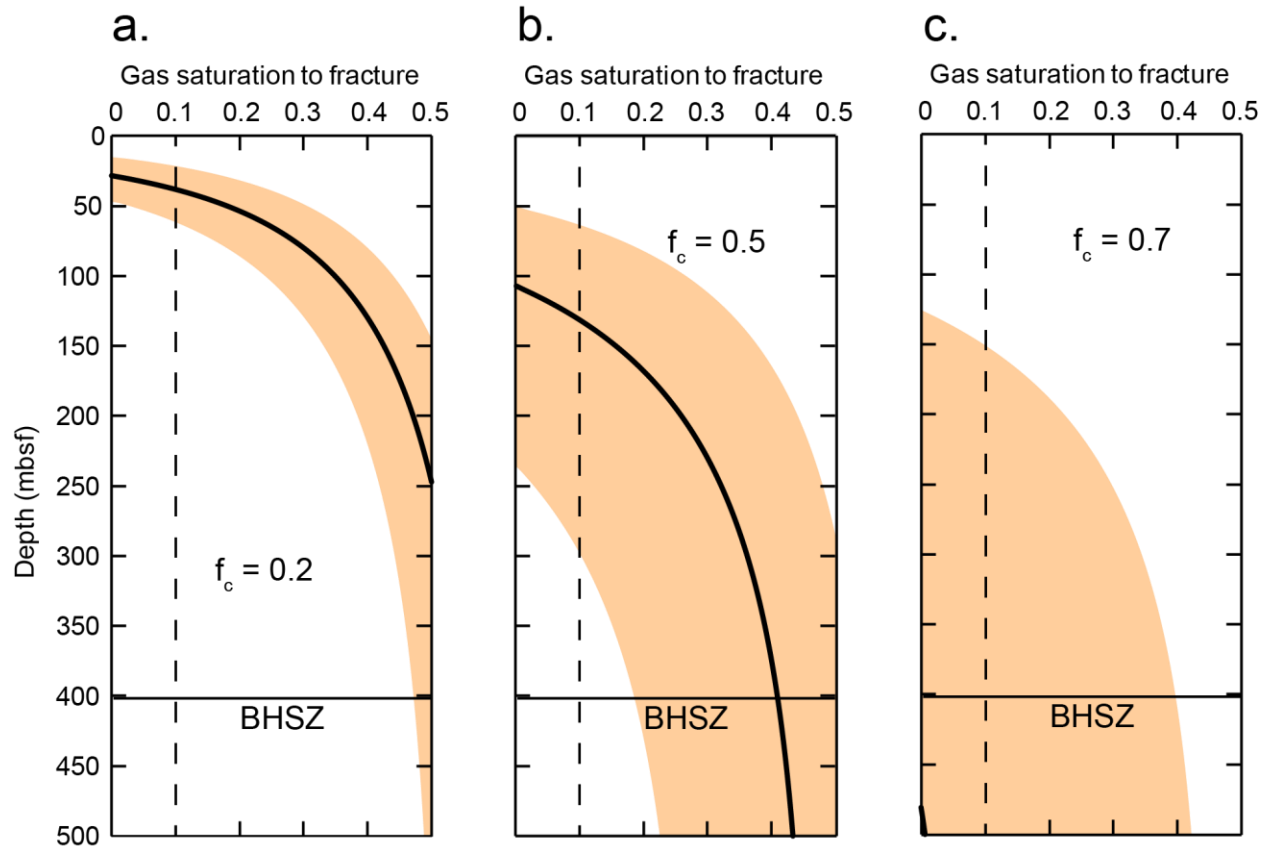
394

395 4. Results

396 *4.1 Generic marine hydrate system*

397 We considered the tensile fracturing behavior of a generic marine hydrate system. The
398 seafloor depth and temperature were 2000 m and 3°C, and the geothermal gradient was
399 40°C/km. These values were selected to represent a deepwater, passive continental margin. The
400 water density and salinity were 1024 kg/m³ and 3.5 wt% NaCl equivalent and the water-phase
401 pressure was assumed hydrostatic. Based on the SI methane hydrate equilibrium temperature-
402 pressure curve obtained from the CSMHYD program [Sloan, 1998], the base of the hydrate
403 stability zone (BHSZ) was located at 403 mbsf.

404 Figure 6 shows the range of gas saturations necessary to form tensile fractures (± 1
405 standard deviation), taking into account the uncertainties in the Brooks-Corey parameters and
406 Hoek-Brown tensile strength estimate. In each panel of Fig. 6, the mobility threshold is marked
407 with a dashed vertical line. Tensile fracturing will be favored over porous flow wherever the gas
408 saturation necessary for fracture (dark black line) is to the left of the mobility threshold line. For
409 sediments with $f_c = 0.2$, fracturing occurs at gas saturations less than 10% shallower than 38
410 mbsf for the median case, indicating that gas accumulation in the shallowest 38 m of sediment
411 will tend to result in tensile fracturing rather than porous flow (Fig. 6a). As f_c increases,
412 fracturing is favored over more of the hydrate stability zone. For $f_c = 0.5$, fracturing is possible in
413 the median case shallower than 132 mbsf (Fig. 6b), and for $f_c = 0.7$ fracturing is possible in the
414 median case over the entire hydrate stability zone (Fig. 6c). Increasing the clay-sized fraction of



415

416 **Figure 6.** Gas saturation required to reach the fracture criterion in our generic passive margin
 417 sediments for clay fractions of 0.2 (a), 0.5 (b), and 0.7 (c). The solid black line represents the
 418 median prediction, while the shaded region shows the uncertainty. The vertical dashed line
 419 indicates the gas mobility threshold. Fracturing will happen whenever the solid black line is to
 420 the left of the vertical dashed line.

421

422 the sediment thus makes gas-driven tensile fracturing more likely. Since the absolute
 423 permeability of marine muds decreases with increasing clay-sized fraction at constant porosity
 424 [Daigle and Scretton, 2015], higher clay-sized fraction will also decrease the rate of excess pore
 425 pressure dissipation, which would further promote tensile fracturing at gas saturations above the
 426 mobility threshold in the case of sufficiently rapid gas evolution from hydrate dissociation or an
 427 external source.

428

429

430 4.2 Fracturing caused by hydrate dissociation at the BHSZ

431 While we have demonstrated the conditions that favor gas-driven tensile fracturing within
432 the hydrate stability zone, a more pertinent question for hydrate-bearing sediments is the
433 potential for gas-driven fracturing at the BHSZ, as this is where hydrate will first dissociate as a
434 result of an increase in the steady-state temperature profile [Ruppel, 2011]. Indeed, many
435 locations around the world already have thick gas columns trapped beneath the BHSZ [Flemings
436 *et al.*, 2003; Hornbach *et al.*, 2004; Tréhu *et al.*, 2004], which raises the possibility that the
437 sediments in these locations may already be near or at the conditions required for tensile failure.

438 We considered a generic passive margin setting in water depths ranging from 500 to 3000
439 m. The seawater density and salinity and geothermal gradient were the same as those assumed in
440 Section 4.1. For the temperature at the sea floor, we interpolated the temperature-depth data
441 presented by Phrampus and Hornbach [2012] based on conductivity-temperature-depth (CTD)
442 casts in the vicinity of the Blake Ridge outside the influence of the Gulf Stream. While these data
443 are specific to Blake Ridge, Phrampus and Hornbach [2012] compared the data to similar data
444 from the eastern Pacific Ocean and found agreement to within 1.5°C, suggesting that these data
445 are representative of a generic sea floor temperature. Using the seafloor temperature, specified
446 geothermal gradient, and hydrostatic pressure, we determined the depth of the BHSZ by
447 comparing the in situ temperature with the equilibrium temperature-pressure data from
448 CSMHYD (Fig. 7a). No hydrate stability zone exists in the sediments at water depths shallower
449 than 523 m, and this water depth represents the updip limit or feather edge of the hydrate
450 stability zone, so called because thickness of the hydrate stability zone within the sediments
451 decreases to zero at this water depth [McIver, 1982; Ruppel, 2011]. At greater water depths, the
452 hydrate stability zone thickens, reaching a thickness of 483 m at 3000 m water depth.

453 Since the tensile strength of marine muds increases with depth, as does the minimum
454 principal stress, greater amounts of gas are required to initiate tensile fractures at the BHSZ in
455 deeper water. For sediments with $f_c = 0.2$, the median gas saturation necessary to fracture at the
456 BHSZ is smaller than 10% only for water depths shallower than 560 m (Fig. 7b), indicating that
457 tensile failure of coarser-grained marine muds at the BHSZ is unlikely except right at the feather
458 edge of the hydrate stability zone. As clay-sized fraction increases, fracturing at the BHSZ
459 becomes easier. At $f_c = 0.5$, the median gas saturation required for fracturing at the BHSZ is less
460 than 10% for water depths shallower than 670 m (Fig. 7c), and 1670 m for $f_c = 0.7$ (Fig. 7d).

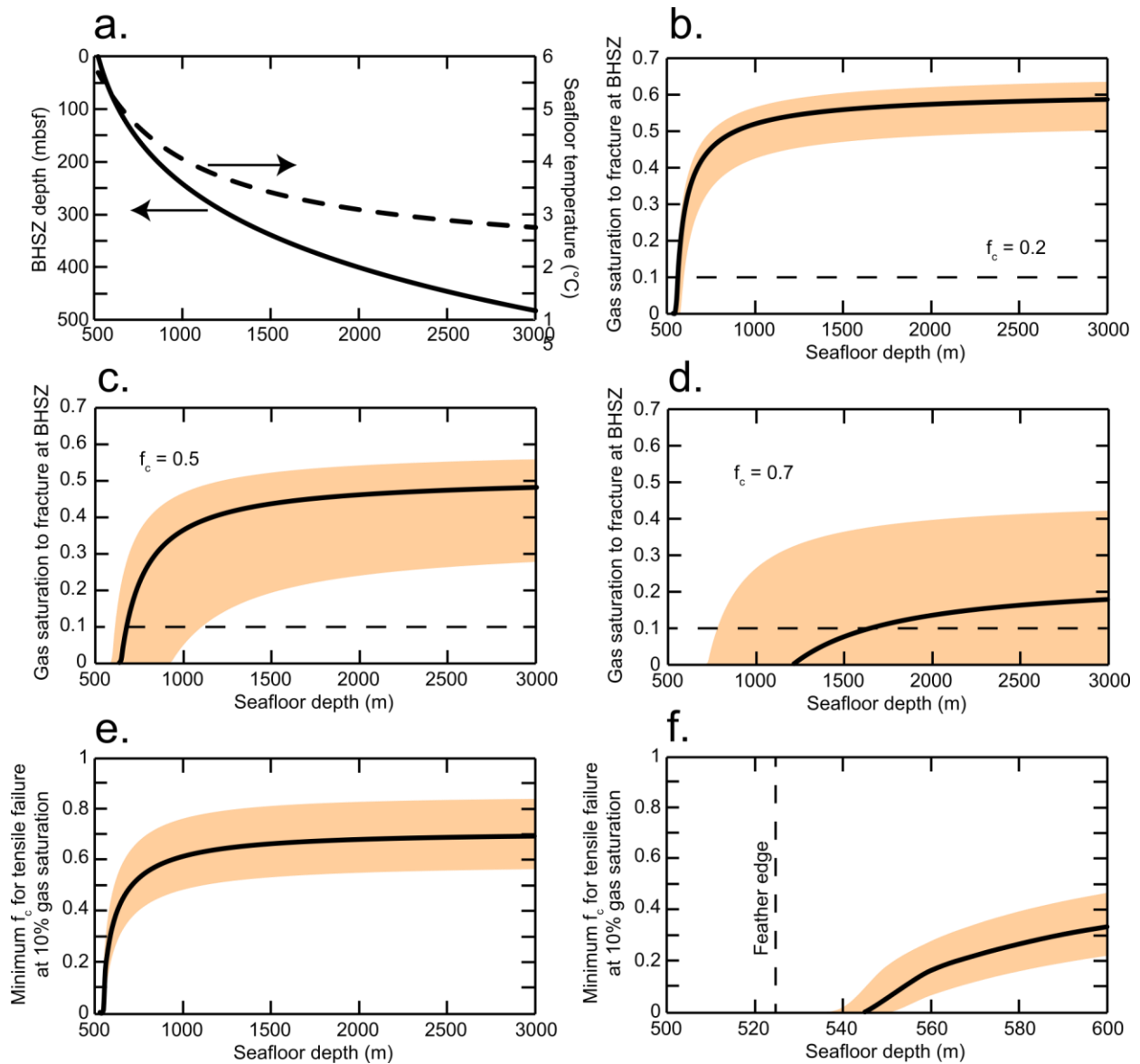
461 We also determined the minimum clay-sized fraction necessary for gas-driven tensile
462 failure at the BHSZ, defined as the value of f_c that yields a median capillary pressure at 10% gas
463 saturation equal to the median fracturing criterion. This value increases rapidly from zero to
464 around 0.6 as water depth increases from 523 m to 1000 m, and increases only slightly with
465 further increase in water depth. For a water depth of 3000 m, the sediments at the BHSZ must
466 have $f_c > 0.69$ for gas-driven tensile failure (Fig. 7e). At the updip limit of the hydrate stability
467 zone, fracturing is much easier. Our modeling suggests that fracturing will always occur,
468 regardless of clay-size fraction, at the feather edge and in water depths as deep as 540 m (Fig.
469 7f).

470

471 5. Discussion

472 *5.1 How much hydrate needs to dissociate?*

473 Gas-driven tensile fracturing is important to understand in the context of the global
474 carbon cycle. Fractures that breach the sea floor and allow venting of gas from below the BHSZ
475 provide important nutrients for chemosynthetic communities at the sea floor [e.g., *Torres et al.*,



476

477 **Figure 7.** (a) Seafloor temperature and BHSZ depth as a function of water depth for our modeled
 478 case. Temperature based on data from *Phrampus and Hornbach* [2012]. The arrows indicate that
 479 BHSZ depth (solid line) is plotted on the left-hand y-axis while seafloor temperature (dashed
 480 line) is plotted on the right-hand y-axis. (b,c,d) Critical gas saturations to cause fracturing at the
 481 BHSZ for clay fractions of 0.2, 0.5, and 0.7. The gas mobility threshold is marked with a dashed
 482 line. (e) Minimum clay fraction that will result in fracturing at the BHSZ at 10% gas saturation.
 483 (f) Close-up of (e) showing the vicinity of the feather edge (523 m seafloor depth; dashed line).
 484 Solid black lines in all plots represent the median prediction, while the shaded regions represent
 485 the uncertainty.

486

487

488

489 2002; Tryon *et al.*, 2002]. Over larger spatial and time scales, gas hydrate can act as a capacitor
490 in the global carbon cycle, holding carbon for long periods of time and releasing it in response to
491 external perturbations [Dickens, 2003]. The factors governing the evolution of gas from hydrates
492 are well understood, but the fate of that gas, including what determines its rate of transfer to the
493 ocean, is not. Gas venting at the sea floor inferred to emanate from dissociating hydrates is
494 observed at many locations worldwide, in response to both postglacial isostatic rebound and
495 ocean temperature changes and anthropogenic warming [Ruppel and Kessler, 2017]. This
496 venting may result from a combination of dissociation-derived gas accumulation and migration
497 of gas from depth and accumulation at the BSHZ [e.g., Daigle *et al.*, 2011; Plaza-Faverola and
498 Keiding, 2019]. Understanding the role of hydrate-derived gas in this process is central to
499 predicting how hydrate systems respond to external perturbations.

500 The question arises, then, about how much hydrate needs to dissociate to generate the gas
501 volumes required to initiate tensile fractures. At standard temperature and pressure, the molar
502 volume of methane gas is roughly 164 times that of sI methane hydrate [Collett *et al.*, 2015], but
503 at in situ conditions this ratio is much smaller. For instance, using the modified Lee-Kesler
504 equation of state for methane described by Duan *et al.* [1992], at the in situ pressure and
505 temperature in the vicinity of the BSHZ at Ocean Drilling Program (ODP) Site 997 on Blake
506 Ridge (roughly 34.5 MPa and 21°C [Ruppel, 1997; Flemings *et al.*, 2003]), the molar volume of
507 methane gas is only about 0.51 times that of sI methane hydrate. At these conditions, the initial
508 hydrate saturation would be nearly twice the corresponding gas saturation following dissociation.
509 In porous media the situation is slightly more complicated since the capillary pressure of the gas
510 phase must also be considered.

511 If porosity does not change upon hydrate dissociation, the hydrate saturation S_h necessary
512 to yield a particular gas saturation S_g is given by

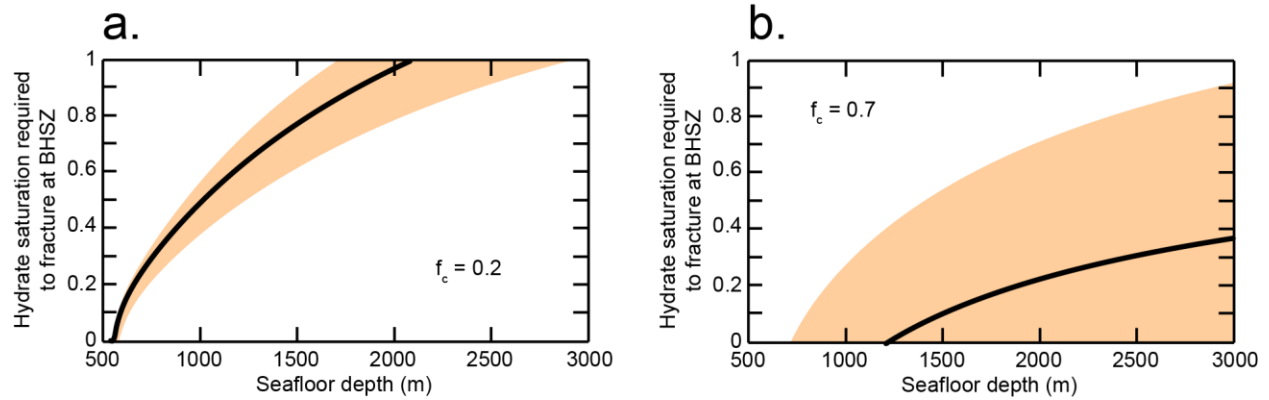
513

$$514 \quad S_h = S_g \frac{V_{m,h}}{V_{m,g}}, \quad (\text{Eq. 13})$$

515

516 where $V_{m,h}$ and $V_{m,g}$ are the molar volumes of hydrate and gas. We considered the hydrate
517 saturation necessary to yield the gas saturation required to generate tensile fracturing at the
518 BHSZ. $V_{m,g}$ was calculated using the equation of state of *Duan et al.* [1992] at the in situ
519 temperature and a gas pressure equal to hydrostatic pressure plus the capillary pressure
520 corresponding to the critical gas saturation for fracture. $V_{m,h}$ was assumed constant and was
521 determined as $1.29 \times 10^{-4} \text{ m}^3/\text{mol}$ based on a molar mass for sI hydrate ($\text{CH}_4 \cdot 5.75\text{H}_2\text{O}$) of 0.1192
522 kg/mol and a hydrate bulk density of 925 kg/m^3 [*Waite et al.*, 2009].

523 Figure 8 shows the hydrate saturations required to generate fractures at $f_c = 0.2$ and $f_c =$
524 0.7 . Since capillary pressures are lower when less clay is present, more gas and correspondingly
525 more dissociated hydrate are required to generate fractures. In water depths greater than 1000 m
526 when $f_c = 0.2$, a hydrate saturation of greater than 50% would need to dissociate to generate a
527 sufficient amount of gas to cause tensile fractures (Fig. 8a). However, the larger capillary
528 pressures in sediments with more clay will reduce the molar volume of methane gas, which
529 means that more hydrate will need to dissociate to generate the required gas saturation. This
530 explains the wide range of required hydrate saturations at $f_c = 0.7$ (Fig. 8b). Hydrate saturations
531 in marine muds rarely exceed 10% except in localized cases [*Boswell and Collett*, 2006], and so
532 it appears unlikely that hydrate dissociation at the BHSZ in deepwater settings (water depths
533 greater than about 1500 m) would lead to gas-driven tensile fracturing, except in cases of



534

535 **Figure 8.** Initial hydrate saturation that would need to dissociate to cause fracturing at the BHSZ
 536 as a function of water depth for clay fractions of 0.2 (a) and 0.7 (b). The solid black lines
 537 represent the median prediction, while the shaded regions represent the uncertainty.
 538

539 localized, high-saturation accumulations of hydrate. On the other hand, near the feather edge,
 540 any amount of dissociated hydrate can lead to tensile fracturing.

541 This analysis assumes that any excess pore pressure that develops following hydrate
 542 dissociation dissipates rapidly. If excess pore pressure is retained at least partially for some time,
 543 this will reduce the molar volume of methane gas and further increase the amount of hydrate
 544 needed to generate the necessary gas saturation. Likewise, we ignore the endothermic nature of
 545 hydrate dissociation [Waite *et al.*, 2009], which would perturb the in situ temperature.

546

547 5.2 Venting at the feather edge

548 Seafloor methane venting has been observed on many continental margins close to the
 549 feather edge where the BHSZ outcrops at the seafloor and may be related to changes in water
 550 temperature or depth on time scales ranging from seasonal to glacial-interglacial, including since
 551 the onset of the Industrial Age [Ruppel and Kessler, 2017]. Changes in ocean temperature will
 552 tend to affect hydrates nearest the seafloor first, and in this context the observed methane venting
 553 near the feather edge is not surprising [e.g., Phrampus and Hornbach, 2012], although it may be

554 possible for gas derived from dissociation downdip of the feather edge or from a deep non-
555 hydrate source to migrate updip [e.g., *Darnell and Flemings, 2015*]. Our calculations indicate
556 that any sediment, regardless of clay-size fraction, is susceptible to tensile failure at the feather
557 edge, and that any amount of hydrate dissociation will preferentially form fractures as the
558 evolved gas vents to the water column. Observable seafloor gas venting at the feather edge does
559 not require very much hydrate to dissociate because of gas expansion. At the pressure and
560 temperature we considered at the feather edge (5.3 MPa, 5.7°C), 1 mol of methane gas occupies
561 3.0 times the volume of 1 mol of methane hydrate. With a seafloor sediment porosity of 0.775
562 based on the *Kominz et al. [2011]* model, dissociation of 1% hydrate saturation would produce
563 23.5 L of methane gas per m³ of sediment. Widespread observations of seafloor methane bubble
564 discharge from discrete vents near the feather edge are consistent with our predictions and
565 require only small amounts of hydrate dissociation to appear. However, we caution that venting
566 near the feather edge is not necessarily an indication of hydrate dissociation, since microbial
567 methanogenesis in sediments outside the hydrate stability zone can still produce gas that can
568 cause fracturing and venting [e.g., *Naudts et al., 2009; Skarke et al., 2014*].

569

570 *5.3 The role of lithologic heterogeneity*

571 The predicted critical gas saturations for tensile failure shown in Figures 6-8 all assume a
572 uniform lithology (i.e., constant f_c) between the BHSZ and seafloor. The marine subsurface is
573 more complicated than this, often exhibiting mixtures of lithologies (clay-rich, silty, sandy) in
574 vertical and lateral successions. At a given porosity, sediments with less clay will be less prone
575 to fracture, and it is conceivable that a propagating fracture may be arrested upon intersecting a
576 coarser-grained layer since the capillary pressure will be lower in the coarser-grained layer. A

577 similar fracture-arresting phenomenon due to contrasts in mechanical properties is well known in
578 lithified sediments, for example hydrocarbon reservoirs [e.g., *Rijken and Cooke, 2001*], and may
579 provide a migration pathway for gas to form hydrates in coarser-grained layers within the
580 hydrate stability zone [*Cook et al., 2008*]. Although the expansion of gas as it rises buoyantly
581 will tend to promote a fracture's propagation once it initiates, extreme cases like chimneys that
582 reach from the BHSZ to the seafloor are likely to form only in relatively homogeneous
583 sediments.

584

585 6. Conclusions

586 We demonstrated that gas-driven tensile fracturing is generally only possible in the
587 shallowest sediments, although the lower depth limit of tensile fracturing increases with
588 increasing clay content. With $f_c = 0.2$, fracturing is only favored in the shallowest 38 m of
589 sediment, but fracturing may be possible to a depth of 132 mbsf when $f_c = 0.5$ and to a depth of
590 nearly 500 mbsf when $f_c = 0.7$. This means that the potential for gas-driven tensile fracturing
591 caused by dissociation of hydrate at the BHSZ is greatest in shallower water, where the BHSZ is
592 closer to the seafloor.

593 Dissociating hydrate at the BHSZ can be a source of gas that can in turn cause tensile
594 failure. We found that in clay-poor sediments ($f_c = 0.2$), more than 20% initial hydrate saturation
595 would need to dissociate to generate gas-driven tensile fractures for all but the very shallowest
596 water depths considered (<600 m). However, when the sediments have more clay, much less
597 dissociated hydrate is necessary. At $f_c = 0.7$, any amount of dissociated hydrate can generate
598 tensile fractures at the BHSZ in water depths as great as 1000 m. Fracturing potential is greatest
599 near the feather edge of the hydrate stability zone: any amount of gas can generate fractures,

600 regardless of the clay-sized fraction. This ease of fracturing combines with significant gas
601 expansion relative to original hydrate volume (roughly a factor of 3) to allow seafloor gas
602 venting near the feather edge with even minor amounts of hydrate dissociation.

603 Our work overall has shown the conditions under which gas-driven tensile fracturing may
604 occur. The results presented here were based on simplifying assumptions and an idealized case
605 of a passive continental margin, and predicting fracturing behavior at specific sites around the
606 world would require more detailed knowledge of many different factors. However, the general
607 conclusion that gas-driven tensile failure is probably a common occurrence near the seafloor and
608 does not require much gas is important to consider in future studies of the source and fate of gas
609 in the shallow marine subsurface.

610

611 Acknowledgments

612 This work was supported by the University of Texas at Austin, and the Laboratory
613 Directed Research and Development program at Sandia National Laboratories. Sandia National
614 Laboratories is a multimission laboratory managed and operated by National Technology and
615 Engineering Solutions of Sandia, LLC., a wholly owned subsidiary of Honeywell International,
616 Inc., for the U.S. Department of Energy's National Nuclear Security Administration under
617 contract DE-NA-0003525. Cook was supported by NSF Award 1752882. The data on which this
618 article is based are available in *Daigle and Dugan* [2014], *Daigle et al.* [2015], *Daigle et al.*
619 [2019], *Hamilton* [1979], *Kominz et al.* [2011], and *Phrampus and Hornbach* [2012].

620

621

622

623 References

- 624 Algar, C. K., & Boudreau, B. P. (2010). Stability of bubbles in a linear elastic medium:
625 Implications for bubble growth in marine sediments. *Journal of Geophysical Research*,
626 *115*(F3), F03012. <https://doi.org/10.1029/2009JF001312>
- 627 Algar, C. K., Boudreau, B. P., & Barry, M. A. (2011). Release of multiple bubbles from cohesive
628 sediments. *Geophysical Research Letters*, *38*, L08606.
629 <https://doi.org/10.1029/2011GL046870>
- 630 Archer, D., Buffett, B., & Brovkin, V. (2009). Ocean methane hydrates as a slow tipping point in
631 the global climate cycle. *Proceedings of the National Academy of Science of the United*
632 *States of America*, *106*(49), 20596-20601. <https://doi.org/10.1073/pnas.0800885105>
- 633 Barry, M. A., Boudreau, B. P., Johnson, B. D., & Reed, A. H. (2010). First-order description of
634 the mechanical fracture behavior of fine-grained surficial marine sediments during gas
635 bubble growth. *Journal of Geophysical Research*, *115*(F4), F04029.
636 <https://doi.org/10.1029/2010JF001833>
- 637 Bear, J. (1972). *Dynamics of fluids in porous media*. New York, NY: Elsevier.
- 638 Best, A. I., Richardson, M. D., Boudreau, B. P., Judd, A. G., Leifer, I., Lyons, A. P., et al.
639 (2006). Shallow seabed methane gas could pose coastal hazard. *Eos*, *87*(22), 213-217.
640 <https://doi.org/10.1029/2006EO220001>
- 641 Bihani, A., & Daigle, H. (2019). On the role of spatially correlated heterogeneity in determining
642 mudrock sealing capacity for CO₂ sequestration. *Marine and Petroleum Geology*, *106*, 116-
643 127. <https://doi.org/10.1016/j.marpetgeo.2019.04.038>
- 644 Bishop, A. W. (1959). The principle of effective stress. *Teknisk Ukeblad*, *39*, 859-863.

645 Boswell, R., & Collett, T. S. (2006). The gas hydrates resource pyramid. *Fire in the Ice*, 6(3), 5-
646 7.

647 Boswell, R., & Collett, T. S. (2011). Current perspectives on gas hydrate resources. *Energy and*
648 *Environmental Science*, 4, 1206-1215. <https://doi.org/10.1039/C0EE00203H>

649 Boudreau, B. P. (2012). The physics of bubbles in surficial, soft, cohesive sediments. *Marine*
650 *and Petroleum Geology*, 38(1), 1-18. <https://doi.org/10.1016/j.marpetgeo.2012.07.002>

651 Boudreau, B. P., Algar, C., Johnson, B. D., Croudace, I., Reed, A., Furukawa, Y., et al. (2005).
652 Bubble growth and rise in soft sediments. *Geology*, 33(6), 517-520.
653 <https://doi.org/10.1130/G21259.1>

654 Brooks, R. H., & Corey, A. T. (1964). *Hydraulic properties of porous media* (Hydrology Paper
655 3). Fort Collins, CO: Colorado State University.

656 Chatzis, I., & Dullien, F. A. L. (1977). Modelling pore structure by 2-D and 3-D networks with
657 application to sandstones. *Journal of Canadian Petroleum Technology*, 16(1), 97-108.
658 <https://doi.org/10.2118/77-01-09>

659 Choi, J.-H., Seol, Y., Boswell, R., & Juanes, R. (2011). X-ray computed-tomography imaging of
660 gas migration in water-saturated sediments: From capillary invasion to conduit opening.
661 *Geophysical Research Letters*, 38(17), L17310. <https://doi.org/10.1029/2011GL048513>

662 Clennell, M. B., Hovland, M., Booth, J. S., Henry, P., & Winters, W. J. (1999). Formation of
663 natural gas hydrates in marine sediments 1. Conceptual model of gas hydrate growth
664 conditioned by host sediment properties. *Journal of Geophysical Research*, 104(B10),
665 22985-23003. <https://doi.org/10.1029/1999JB900175>

666 Collett, T., Bahk, J., Baker, R., Boswell, R., Divins, D., Frye, M., et al. (2015). Methane hydrates
667 in nature – current knowledge and challenges. *Journal of Chemical & Engineering Data*,
668 60(2), 319-329. <https://doi.org/10.1021/je500604h>

669 Cook, A. E., & Goldberg, D. (2008). Extent of gas hydrate filled fracture planes: Implications for
670 in situ methanogenesis and resource potential. *Geophysical Research Letters*, 35(15),
671 L15302. <https://doi.org/10.1029/2008GL034587>

672 Cook, A. E., Goldberg, D., & Kleinberg, R. L. (2008). Fracture-controlled gas hydrate systems in
673 the northern Gulf of Mexico. *Marine and Petroleum Geology*, 25, 932-941.
674 <https://doi.org/10.1026/j.marpetgeo.2008.01.013>

675 Cook, A. E., Goldberg, D. S., & Malinverno, A. (2014). Natural gas hydrates occupying
676 fractures: A focus on non-vent sites on the Indian continental margin and the northern Gulf
677 of Mexico. *Marine and Petroleum Geology*, 58(A), 278-291.
678 <https://doi.org/10.1016/j.marpetgeo.2014.04.013>

679 Coussy, O., 2004. *Poromechanics*. Chichester, U. K.: John Wiley & Sons.

680 Coussy, O., 2007. Revisiting the constitutive equations of unsaturated porous solids using a
681 Lagrangian saturation concept. *International Journal for Numerical and Analytical Methods*
682 *in Geomechanics*, 31, 1675-1694. <https://doi.org/10.1002/nag.613>

683 Daigle, H., & Dugan, B. (2010a). Effects of multiphase methane supply on hydrate accumulation
684 and fracture generation. *Geophysical Research Letters*, 37(20), L20301.
685 <https://doi.org/10.1029/2010GL044970>

686 Daigle, H., & Dugan, B. (2010b). Origin and evolution of fracture-hosted methane hydrate
687 deposits. *Journal of Geophysical Research*, 115(B11), B11103.
688 <https://doi.org/10.1029/2010JB007492>

689 Daigle, H., & Dugan, B. (2011). Capillary controls on methane hydrate distribution and
690 fracturing in advective systems. *Geochemistry, Geophysics, Geosystems*, 12(1), Q01003.
691 <https://doi.org/10.1029/2010GC003392>

692 Daigle, H., & Dugan, B. (2014). Data report: permeability, consolidation, stress state, and pore
693 system characteristics of sediments from Sites C0011, C0012, and C0018 of the Nankai
694 Trough. *Proceedings of the Integrated Ocean Drilling Program*, 333, 1-23.
695 <https://doi.org/10.2204/iodp.proc.333.201.2014>

696 Daigle, H., & Screatton, E. J. (2015). Predicting the permeability of sediments entering
697 subduction zones. *Geophysical Research Letters*, 42(13), 5219-5226.
698 <https://doi.org/10.1002/2015GL064542>

699 Daigle, H., Bangs, N. L., & Dugan, B. (2011). Transient hydraulic fracturing and gas release in
700 methane hydrate settings: A case study from southern Hydrate Ridge. *Geochemistry,*
701 *Geophysics, Geosystems*, 12(12), Q12022. <https://doi.org/10.1029/2011GC003841>

702 Daigle, H., Ghanbarian, B., Henry, P., & Conin, M. (2015). Universal scaling of the formation
703 factor in clays: Example from the Nankai Trough. *Journal of Geophysical Research Solid*
704 *Earth*, 120(11), 7361-7375. <https://doi.org/10.1002/2015JB012262>

705 Daigle, H., Reece, J. S., & Flemings, P. B. (2019). Evolution of the percolation threshold in
706 muds and mudrocks during burial. *Geophysical Research Letters*, 46(14), 8064-8073.
707 <https://doi.org/10.1029/2019GL083723>

708 Darnell, K. N., & Flemings, P. B. (2015). Transient seafloor venting on continental slopes from
709 warming-induced methane hydrate dissociation. *Geophysical Research Letters*, 42(24),
710 10765-10772. <https://doi.org/10.1002/2015GL067012>

711 Diaz, C. E., Chatzis, I., & Dullien, F. A. L. (1987). Simulation of capillary pressure curves using
712 bond correlated site percolation on a simple cubic network. *Transport in Porous Media*, 2(3),
713 215-240. <https://doi.org/10.1007/BF00165783>

714 Dickens, G. R. (2003). Rethinking the global carbon cycle with a large, dynamic and microbially
715 mediated gas hydrate capacitor. *Earth and Planetary Science Letters*, 213(3-4), 169-183.
716 [https://doi.org/10.1016/S0012-821X\(03\)00325-X](https://doi.org/10.1016/S0012-821X(03)00325-X)

717 Duan, Z., Møller, N., & Weare, J. H. (1992). An equation of state for the CH₄-CO₂-H₂O system:
718 I. Pure systems from 0 to 1000°C and 0 to 8000 bar. *Geochimica et Cosmochimica Acta*,
719 56(7), 2605-2617. [https://doi.org/10.1016/0016-7037\(92\)90347-L](https://doi.org/10.1016/0016-7037(92)90347-L)

720 Dugan, B., & Germaine, J. T. (2009). Data report: strength characteristics of sediments from
721 IODP Expedition 308, Sites U1322 and U1324. *Proceedings of the Integrated Ocean*
722 *Drilling Program*, 308, 1-13. <https://doi.org/10.2204/iodp.proc.308.210.2009>

723 Eaton, B. A. (1969). Fracture gradient prediction and its application in oilfield operations.
724 *Journal of Petroleum Technology*, 21(10), 1353-1360. <https://doi.org/10.2118/2163-PA>

725 Ewing, R. P., & Gupta, S. C. (1993). Modeling percolation properties of random media using a
726 domain network. *Water Resources Research*, 29(9), 3169-3178.
727 <https://doi.org/10.1029/93WR01496>

728 Fauria, K. E., & Rempel, A. W. (2011). Gas invasion into water-saturated, unconsolidated
729 porous media: Implications for gas hydrate reservoirs. *Earth and Planetary Science Letters*,
730 312(1-2), 188-193. <https://doi.org/10.1016/j.epsl.2011.09.042>

731 Flemings, P. B., Liu, X., & Winters, W. J. (2003). Critical pressure and multiphase flow in Blake
732 Ridge gas hydrates. *Geology*, 31(12), 1057-1060. <https://doi.org/10.1130/g19863.1>

733 Ginsburg, G. D., & Soloviev, V. A. (1997). Methane migration within the submarine gas-hydrate
734 stability zone under deep-water conditions. *Marine Geology*, 137(1-2), 49-57.
735 [https://doi.org/10.1016/S0025-3227\(96\)00078-3](https://doi.org/10.1016/S0025-3227(96)00078-3)

736 Griffith, A. A. (1921). The phenomena of rupture and flow in solids. *Philosophical Transactions*
737 *of the Royal Society A*, 221, 582-593. <https://doi.org/10.1098/rsta.1921.0006>

738 Hamilton, E. L. (1979). V_p/V_s and Poisson's ratios in marine sediments and rocks. *Journal of the*
739 *Acoustical Society of America*, 66(4), 1093-1101. <https://doi.org/10.1121/1.383344>

740 Henry, P., Thomas, M., & Clennell, M.B. (1999). Formation of natural gas hydrates in marine
741 sediments 2. Thermodynamic calculations of stability conditions in porous sediments.
742 *Journal of Geophysical Research*, 104(B10), 23005-23022.
743 <https://doi.org/10.1029/1999JB900167>

744 Hildenbrand, A., Schlömer, S., & Krooss, B. M. (2002). Gas breakthrough experiments on fine-
745 grained sedimentary rocks. *Geofluids*, 2(1), 3-23. [https://doi.org/10.1046/j.1468-](https://doi.org/10.1046/j.1468-8123.2002.00031.x)
746 [8123.2002.00031.x](https://doi.org/10.1046/j.1468-8123.2002.00031.x)

747 Hildenbrand, A., Schlömer S., Krooss, B. M., & Littke, R. (2004). Gas breakthrough
748 experiments on politic rocks: comparative study with N₂, CO₂ and CH₄. *Geofluids*, 4(1), 61-
749 80. <https://doi.org/10.1111/j.1468-8123.2004.00073.x>

750 Hirasaki, G. J. (1991). Wettability: fundamentals and surface forces. *SPE Formation Evaluation*,
751 6(2), 217-226. <https://doi.org/10.2118/17367-PA>

752 Hoek, E. (2006). *Practical rock engineering*. Retrieved from
753 [https://www.rocscience.com/assets/resources/learning/hoek/Practical-Rock-Engineering-](https://www.rocscience.com/assets/resources/learning/hoek/Practical-Rock-Engineering-Full-Text.pdf)
754 [Full-Text.pdf](https://www.rocscience.com/assets/resources/learning/hoek/Practical-Rock-Engineering-Full-Text.pdf).

755 Hoek, E., & Brown, E. T. (1997). Practical estimates of rock mass strength. *International*
756 *Journal of Rock Mechanics and Mining Sciences*, 34(8), 1165-1186.
757 [https://doi.org/10.1016/S1365-1609\(97\)80069-X](https://doi.org/10.1016/S1365-1609(97)80069-X)

758 Holtzman, R., & Juanes, R. (2011). Thermodynamic and hydrodynamic constraints on
759 overpressure caused by hydrate dissociation: A pore-scale model. *Geophysical Research*
760 *Letters*, 38(14), L14308. <https://doi.org/10.1029/2011GL047937>

761 Hornbach, M. J., Saffer, D. M., & Holbrook, W. S. (2004). Critically pressured free-gas
762 reservoirs below gas-hydrate provinces. *Nature*, 427, 142-144.
763 <https://doi.org/10.1038/nature02172>

764 Hustoft, S., Büinz, S., Mienert, J., & Chand, S. (2009). Gas hydrate reservoir and active methane-
765 venting province in sediments on < 20 Ma young oceanic crust in the Fram Strait, offshore
766 NW-Svalbard. *Earth and Planetary Science Letters*, 284(1-2), 12-24.
767 <https://doi.org/10.1016/j.epsl.2009.03.038>

768 Ingram, G. M., & Urai, J. L. (1999). Top-seal leakage through faults and fractures: the role of
769 mudrock properties. In A. C. Aplin, A. J. Fleet, J. H. S. Macquaker (Eds.), *Muds and*
770 *mudstones: physical and fluid flow properties*, Geological Society, London, Special
771 Publications (Vol. 158, pp. 125-135). London: The Geological Society of London.
772 <https://doi.org/10.1144/GSL.SP.1999.158.01.10>

773 Jain, A. K., & Juanes, R. (2009). Preferential mode of gas invasion in sediments: Grain-scale
774 mechanistic model of coupled multiphase fluid flow and sediment mechanics. *Journal of*
775 *Geophysical Research*, 114(B8), B08101. <https://doi.org/10.1029/2008JB006002>

776 James, R. H., Bousquet, P., Bussmann, I., Haeckel, M., Kipfer, R., Leifer, I., et al. (2016).
777 Effects of climate change on methane emissions from seafloor sediments in the Arctic

778 Ocean: A review. *Limnology and Oceanography*, 61, S283-S299.
779 <https://doi.org/10.1002/lno.10307>

780 Jin, Z., Johnson, S. E., & Cook, A. E. (2015). Crack extension induced by dissociation of
781 fracture-hosted methane gas hydrate. *Geophysical Research Letters*, 42(20), 8522-8529.
782 <https://doi.org/10.1002/2015GL066060>

783 Johnson, B. D., Barry, M. A., Boudreau, B. P., Jumars, P. A., & Dorgan, K. M. (2012). In situ
784 tensile fracture toughness of surficial cohesive marine sediments. *Geo-Marine Letters*, 32(1),
785 39-48. <https://doi.org/10.1007/s00367-011-0243-1>

786 Johnson, B. D., Boudreau, B. P., Gardiner, B. S., & Maass, R. (2002). Mechanical response of
787 sediments to bubble growth. *Marine Geology*, 187(3-4), 347-363.
788 [https://doi.org/10.1016/s0025-3227\(02\)00383-3](https://doi.org/10.1016/s0025-3227(02)00383-3)

789 Kominz, M. A., Patterson, K., & Odette, D. (2011). Lithology dependence of porosity in slope
790 and deep marine sediments. *Journal of Sedimentary Research*, 81(10), 730-742.
791 <https://doi.org/10.2110/jsr.2011.60>

792 Larson, R. G., & Morrow, N. R. (1981). Effects of sample size on capillary pressures in porous
793 media. *Powder Technology*, 30(2), 123-138. [https://doi.org/10.1016/0032-5910\(81\)80005-8](https://doi.org/10.1016/0032-5910(81)80005-8)

794 Lenormand, R., Zarcone, C., & Sarr, A. (1983). Mechanisms of the displacement of one fluid by
795 another in a network of capillary ducts. *Journal of Fluid Mechanics*, 135, 337-353.
796 <https://doi.org/10.1017/S0022112083003110>

797 Leverett, M. C. (1941). Capillary behavior in porous solids. *Transactions of the AIME*, 142(1),
798 152-169. <https://doi.org/10.2118/941152-G>

799 Liu, X., & Flemings, P. B. (2007). Dynamic multiphase flow model of hydrate formation in
800 marine sediments. *Journal of Geophysical Research*, *112*(B3), B03101.
801 <https://doi.org/10.1029/2005JB004227>

802 Maslin, M., Owen, M., Betts, R., Day, S., Dunkley Jones, T., & Ridgwell, A. (2010). Gas
803 hydrates: past and future geohazard? *Philosophical Transactions of the Royal Society A*,
804 *368*(1919), 2369-2393. <https://doi.org/10.1098/rsta.2010.0065>

805 McIver, R. D. (1982). Role of naturally occurring gas hydrates in sediment transport. *AAPG*
806 *Bulletin*, *66*(6), 789-792. <https://doi.org/10.1306/03b5a318-16d1-11d7-8645000102c1865d>

807 Moses, G. G., Rao, S. N., & Rao, P. N. (2003). Undrained strength behaviour of a cemented
808 marine clay under monotonic and cyclic loading. *Ocean Engineering*, *30*(14), 1765-1789.
809 [https://doi.org/10.1016/S0029-8018\(03\)00018-0](https://doi.org/10.1016/S0029-8018(03)00018-0)

810 Natzeband, G. L., Hübscher, C. P., Gajewski, D., Grobys, J. W. G., & Bialas, J. (2005). Seismic
811 velocities from the Yaquina forearc basin off Peru: evidence for free gas within the gas
812 hydrate stability zone. *International Journal of Earth Sciences*, *94*(3), 420-432.
813 <https://doi.org/10.1007/s00531-005-0483-2>

814 Naudts, L., De Batist, M., Greinert, J., & Artemov, Y. (2009). Geo- and hydro-acoustic
815 manifestations of shallow gas and gas seeps in the Dnepr paleodelta, northwestern Black Sea.
816 *The Leading Edge*, *28*(9), 1030-1040. <https://doi.org/10.1190/1.3236372>

817 Nimblett, J., & Ruppel, C. (2003). Permeability evolution during the formation of gas hydrates in
818 marine sediments. *Journal of Geophysical Research*, *108*(B9), 2420.
819 <https://doi.org/10.1029/2001JB001650>

820 Nuth, M., & Laloui, L. (2008). Effective stress concept in unsaturated soils: Clarification and
821 validation of a unified framework. *International Journal for Numerical and Analytical*
822 *Methods in Geomechanics*, 32(7), 771-801. <https://doi.org/10.1002/nag.645>

823 Phrampus, B. J., & Hornbach, M. J. (2012). Recent changes to the Gulf Stream causing
824 widespread gas hydrate destabilization. *Nature*, 490, 527-530.
825 <https://doi.org/10.1038/nature11528>

826 Plaza-Faverola, A., & Keiding, M. (2019). Correlation between tectonic stress regimes and
827 methane seepage on the western Svalbard margin. *Solid Earth*, 10, 79-94.
828 <https://doi.org/10.5194/se-10-79-2019>

829 Purcell, W. R. (1949). Capillary pressures – their measurement using mercury and the
830 calculation of permeability therefrom. *Journal of Petroleum Technology*, 1(2), 39-48.
831 <https://doi.org/10.2118/949039-g>

832 Rees, E. V. L., Priest, J. A., & Clayton, C. R. I. (2011). Thermodynamic and hydrodynamic
833 constraints on overpressure caused by hydrate dissociation: A pore-scale model. *Marine and*
834 *Petroleum Geology*, 28(7), 1283-1293. <https://doi.org/10.1016/j.marpetgeo.2011.03.015>

835 Rempel, A. W. (2011). A model for the diffusive growth of hydrate saturation anomalies in
836 layered sediments. *Journal of Geophysical Research*, 116(B10), B10105.
837 <https://doi.org/10.1029/2011JB008484>

838 Reynolds, J. M. (1997). *An introduction to applied and environmental geophysics*. Chichester, U.
839 K.: John Wiley.

840 Rijken, P., & Cooke, M. L. (2001). Role of shale thickness on vertical connectivity of fractures:
841 application of crack-bridging theory to the Austin Chalk, Texas. *Tectonophysics*, 337(1-2),
842 117-133. [https://doi.org/10.1016/S0040-1951\(01\)00107-X](https://doi.org/10.1016/S0040-1951(01)00107-X)

843 Ruppel, C. (1997). Anomalously cold temperatures observed at the base of the gas hydrate
844 stability zone on the U.S. Atlantic passive margin. *Geology*, 25(8), 699-702.
845 [https://doi.org/10.1130/0091-7613\(1997\)025%3C0699:ACTOAT%3E2.3.CO;2](https://doi.org/10.1130/0091-7613(1997)025%3C0699:ACTOAT%3E2.3.CO;2)

846 Ruppel, C. D. (2011). Methane hydrates and contemporary climate change. *Nature Education*
847 *and Knowledge*, 3(10), 29.

848 Ruppel, C. D., & Kessler, J. D. (2017). The interaction of climate change and methane hydrates.
849 *Reviews of Geophysics*, 55(1), 126-168. <https://doi.org/10.1002/2016RG000534>

850 Sahimi, M. (2011). *Flow and transport in porous media and fractured rock*, 2nd edition.
851 Weinheim, Germany: Wiley-VCH.

852 Sassen, R., Losh, S. L., Cathles, L., Roberts, H. H., Whelan, J. K., Milkov, A. V., et al. (2001).
853 Massive vein-filling gas hydrate: relation to ongoing gas migration from the deep subsurface
854 in the Gulf of Mexico. *Marine and Petroleum Geology*, 18(5), 551-560.
855 [https://doi.org/10.1016/S0264-8172\(01\)00014-9](https://doi.org/10.1016/S0264-8172(01)00014-9)

856 Schowalter, T. T. (1979). Mechanics of secondary hydrocarbon migration and entrapment.
857 *AAPG Bulletin*, 63(5), 723-760. [https://doi.org/10.1306/2f9182ca-16ce-11d7-](https://doi.org/10.1306/2f9182ca-16ce-11d7-8645000102c1865d)
858 [8645000102c1865d](https://doi.org/10.1306/2f9182ca-16ce-11d7-8645000102c1865d)

859 Schumann, K., Behrmann, J. H., Stipp, M., Yamamoto, Y., Kitamura, Y., & Lempp, C. (2014).
860 Geotechnical behavior of mudstones from the Shimanto and Boso accretionary complexes,
861 and implications for the Nankai accretionary prism. *Earth, Planets and Space*, 66, 129.
862 <https://doi.org/10.1186/1880-5981-66-129>

863 Silva, A., Baxter, C., Bryant, W., Bradshaw, A., & LaRosa, P. (2000). *Stress-strain behavior and*
864 *stress state of Gulf of Mexico clays in relation to slope processes*. Paper presented at 2000

865 Offshore Technology Conference, Offshore Technology Conference, Houston, TX.
866 <https://doi.org/10.4043/12091-MS>

867 Sloan, E. D. (1998). *Clathrate hydrates of natural gases* (2nd ed.). New York, NY: Marcel
868 Dekker.

869 Stranne, C., O'Regan, M., & Jakobsson, M. (2017). Modeling fracture propagation and seafloor
870 gas release during seafloor warming-induced hydrate dissociation. *Geophysical Research*
871 *Letters*, 44(16), 8510-8519. <https://doi.org/10.1002/2017GL074349>

872 Sultan, N., Bohrmann, G., Ruffine, L., Pape, T., Riboulot, V., Colliat, J.-L., et al. (2014).
873 Pockmark formation and evolution in deep water Nigeria: Rapid hydrate growth versus slow
874 hydrate dissolution. *Journal of Geophysical Research*, 119(4), 2679-2694.
875 <https://doi.org/10.1002/2013JB010546>

876 Sun, Y., Wu, S., Dong, D., Lüdmann, T., & Gong, Y. (2012). Gas hydrates associated with gas
877 chimneys in fine-grained sediments of the northern South China Sea. *Marine Geology*, 311-
878 314, 32-40. <https://doi.org/10.1016/j.margeo.2012.04.003>

879 Torres, M. E., McManus, J., Hammond, D. E., de Angelis, M. A., Heeschen, K. U., Colbert, S.
880 L., et al. (2002). Fluid and chemical fluxes in and out of sediments hosting methane hydrate
881 deposits on Hydrate Ridge, OR, I: Hydrological provinces. *Earth and Planetary Science*
882 *Letters*, 201, 525-540. [https://doi.org/10.1016/S0012-821X\(02\)00733-1](https://doi.org/10.1016/S0012-821X(02)00733-1)

883 Tréhu, A. M., Flemings, P. B., Bangs, N. L., Chevallier, J., Gràcia, E., Johnson, J. E., et al.
884 (2004). Feeding methane vents and gas hydrate deposits at south Hydrate Ridge. *Geophysical*
885 *Research Letters*, 31, L23310. <https://doi.org/10.1029/2004GL021286>

886 Tryon, M. D., Brown, K. M., & Torres, M. E. (2002). Fluid and chemical fluxes in and out of
887 sediments hosting methane hydrate deposits on Hydrate Ridge, OR, I: Hydrological

888 processes. *Earth and Planetary Science Letters*, 201, 541-557.
889 [https://doi.org/10.1016/S0012-821X\(02\)00732-X](https://doi.org/10.1016/S0012-821X(02)00732-X)

890 Warpinski, N. R., & Branagan, P. T. (1989). Altered-stress fracturing. *Journal of Petroleum*
891 *Technology*, 41(9), 990-997. <https://doi.org/10.2118/17533-PA>

892 Warpinski, N. R., & Teufel, L. W. (1987). Influence of geologic discontinuities on hydraulic
893 fracture propagation. *Journal of Petroleum Technology*, 39(2), 209-220.
894 <https://doi.org/10.2118/13224-PA>

895 Weinberger, J. L., & Brown, K. M. (2006). Fracture networks and hydrate distribution at Hydrate
896 Ridge, Oregon. *Earth and Planetary Science Letters*, 245, 123-136.
897 <https://doi.org/10.1016/j.epsl.2006.03.012>

898 Wojtanowicz, A. K., Bourgoyne, A. T., Zhou, D., & Bender, K. (2000). *Strength and fracture*
899 *gradients for shallow marine sediments* (Final Technical Report). Herndon, VA: U. S.
900 Department of Interior.

901 Wood, W. T., Gettrust, J. F., Chapman, N. R., Spence, G. D., & Hyndman, R. D. (2002).
902 Decreased stability of methane hydrates in marine sediments owing to phase-boundary
903 roughness. *Nature*, 420, 656-660. <https://doi.org/10.1038/nature01263>

904 Waite, W. F., Santamarina, J. C., Cortes, D. D., Dugan, B., Espinoza, D. N., Germaine, J. T., et
905 al. (2009). Physical properties of hydrate-bearing sediments. *Reviews of Geophysics*, 47,
906 RG4003. <https://doi.org/10.1029/2008RG000279>

907 Washburn, E. W. (1921). The dynamics of capillary flow. *Physical Review*, 17(3), 273-283.
908 <https://doi.org/10.1103/PhysRev.17.273>

909 Xu, W., & Germanovich, L. N. (2006). Excess pore pressure resulting from methane hydrate
910 dissociation in marine sediments: A theoretical approach. *Journal of Geophysical Research*,
911 *111*(B1), B01104. <https://doi.org/10.1029/2004JB003600>

912 Yan, C., Deng, J., Lai, X., Li, X., & Feng, Y. (2015). Borehole stability analysis in deepwater
913 shallow sediments. *Journal of Energy Resources Technology*, *137*(1), 012901.
914 <https://doi.org/10.1115/1.4027564>

915 You, K., Flemings, P. B., Malinverno, A., Collett, T. S., & Darnell, K. (2019). Mechanisms of
916 methane hydrate formation in geological systems. *Reviews of Geophysics*, *57*(4), 1146-1196.
917 <https://doi.org/10.1029/2018RG000638>

918 Zoback, M. D. (2007). *Reservoir geomechanics*. Cambridge, U. K.: Cambridge University Press.

919 Zühlsdorff, L., & Spiess, V. (2004). Three-dimensional seismic characterization of a venting site
920 reveals compelling indications of natural hydraulic fracturing. *Geology*, *32*(2), 101-104.
921 <https://doi.org/10.1130/G19993.1>

922

923

924

925

926

927

928

929

930

931

Symbol	Definition	Dimensions
c_u	Unconfined compressive strength	M/LT ²
f_c	Mass fraction of solid matrix composed of clay-sized grains	M/M
m_i	Hoek-Brown constant	-
P_c	Capillary pressure	M/LT ²
P_e	Capillary entry pressure	M/LT ²
P_g	Gas phase pressure	M/LT ²
P_w	Water phase pressure	M/LT ²
r	Pore radius	L
S_g	Gas saturation	L ³ /L ³
S_h	Hydrate saturation	L ³ /L ³
S_w	Water saturation	L ³ /L ³
S_{wi}	Irreducible wetting phase saturation	L ³ /L ³
T	Tensile strength	M/LT ²
$V_{m,g}$	Gas molar volume	L ³ /mol
$V_{m,h}$	Hydrate molar volume	L ³ /mol
V_p	Compressional wave velocity	L/T
z	Depth below seafloor	L
γ	Gas-water interfacial tension	M/T ²
$\gamma_{CH_4,W}$	Methane-water interfacial tension	M/T ²
$\gamma_{Hg,V}$	Mercury-vacuum interfacial tension	M/T ²
$\theta_{CH_4,W}$	Contact angle of methane-water interface on solid grains	-
$\theta_{Hg,V}$	Contact angle of mercury-vacuum interface on solid grains	-
λ	Pore-size parameter	-
ν	Poisson's ratio	-
σ_3	Minimum principal stress	M/LT ²
σ_h	Total horizontal stress	M/LT ²
σ_h'	Horizontal effective stress	M/LT ²
σ_v	Total vertical stress	M/LT ²
σ_v'	Vertical effective stress	M/LT ²
ϕ	Porosity	L ³ /L ³

932 **Table 1.** Nomenclature